Harnessing Mechanical Instabilities in the Development of an Efficient Soft Pump for an Artificial Heart Ventricle Simulator

Lucrezia Lorenzon, *Associate Member, IEEE*, Alessandro Lucantonio, Leone Costi, Debora Zrinscak, Luca Arleo, and Matteo Cianchetti, *Member, IEEE*

***Abstract*—While mechanical instabilities were traditionally considered as failure events, triggering them in a controlled fashion recently paved the way to novel functionalities and improved performance, especially in systems made of soft materials. In this article, we present a novel cable-driven compliant mechanism whose pumping function is based on mechanical instabilities. Specifically, the cables are arranged in helices wrapped around a soft shell chamber that hosts the fluid, and upon pulling, they cause its dramatic volumetric reduction by inducing a torsional instability that maximizes the pumping action. We introduce a geometrical model to describe the deformation kinematics of the soft pump and a finite element model to investigate the detailed postbuckling behavior of the shell. Both models show very good agreement with the experiments. The computational model allowed us to perform a parametric study of the behavior of the soft pump as a function of the number of turns of the cables and their displacement upon pulling. Finally, we demonstrate experimentally the applicability of our soft pump as an artificial ventricle simulator, since the pumped volumes at physiologically relevant afterload pressures approach those found in left and right human ventricles.**

***Index Terms*—Finite element model (FEM), heart ventricle simulator, mechanical instabilities, soft artificial heart, soft pump, soft robotic artificial ventricle.**

I. Introduction

IN THE past 15 years, soft robotics paved the way toward the design of smart systems capable of dexterous motion [1], [2], collaborative behavior [3], [4], and biomimicry [5] in an unprecedented manner. Advancements in material science and fabrication technologies enabled the use of soft polymeric materials, triggering new design possibilities. Researchers, indeed, started to engineer specific material characteristics to enhance the overall performance. Tuning mechanical and topological properties, for example, enabled the development of smart robotic systems based on metamaterials [6], [7], [8]. Increased efficiency was highlighted in both natural and robotic structures when the elastic properties were combined with a programmed actuation pattern [9].

Moreover, recently, mechanical instabilities and buckling events took on a whole different meaning, becoming synonyms of motion amplification techniques instead of symptoms of structural failure. For example, snap-through instabilities were presented as motion strategies for soft actuators [10], as well as structural buckling enabled the linear motion of vacuum-based systems [11], [12], [13], [14].

These mechanical principles have several interesting applications: Rothermund et al. [15], for example, presented a soft valve able to switch between two states, based on mechanical instabilities. Shim et al. [16] introduced a shell structure able to reduce its volume when undergoing buckling under pressure loading, thus enabling encapsulation.

While mechanical instabilities have been previously explored as motion strategies and structural changes, in this work, we demonstrate how mechanical instabilities can be introduced in the design of a novel soft pump, greatly increasing its pumping performance. With respect to the state-of-the-art, this is the first example of a soft pump whose pumping principle relies on torsional mechanical instabilities. Moreover, although the proposed approach is widely applicable in different application scenarios, in this work, we design a soft pump that can be readily used as a heart ventricle simulator that replicates the performances of a human left or right heart ventricle in terms of pumped volume at physiological afterload pressure. In particular, torsional mechanical instabilities were exploited in this context, and for the first time, to introduce large deformations and quick dynamics, that enabled the achievement of optimal pumping performances.

Over the past decade, various operational principles have been explored for developing soft peristaltic pumps with performance levels that match with the human heart. Initially, the soft pumps

Manuscript received 15 March 2023; revised 16 October 2023; accepted 3 December 2023. Date of publication 26 January 2024; date of current version 18 April 2024. Recommended by Technical Editor G. Berselli and Senior Editor G. Berselli. This work was supported by the European Commission through the Hybrid Heart Project under Grant 767195. *(Corresponding author: Lucrezia Lorenzon.)*

The authors are with the The BioRobotics Institute, Scuola Superiore Sant'Anna, 56025 Pisa, Italy, and also with the Department of Excellence in Robotics & AI, Scuola Superiore Sant'Anna, 56127 Pisa, Italy (e-mail: lucrezia.lorenzon@santannapisa.it; a.lucantonio@mpe.au.dk; lc830@eng.cam.ac.uk; debora.zrinscak@artes4.it; luca.arleo@santannapisa.it; matteo.cianchetti@santannapisa.it).

This article has supplementary material provided by the authors and color versions of one or more figures available at https://doi.org/10.1109/TMECH.2023.3345529.

Digital Object Identifier 10.1109/TMECH.2023.3345529

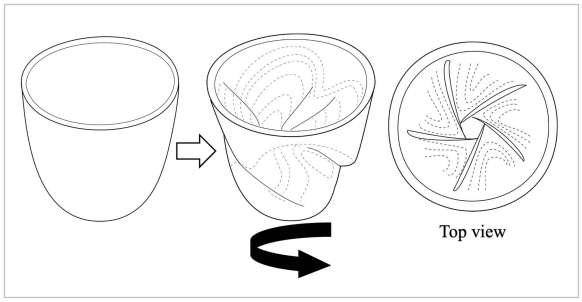

Fig. 1. Actuation concept: (Left) the undeformed shell; (right) torsional deformation of the soft shell induced by helical actuators.

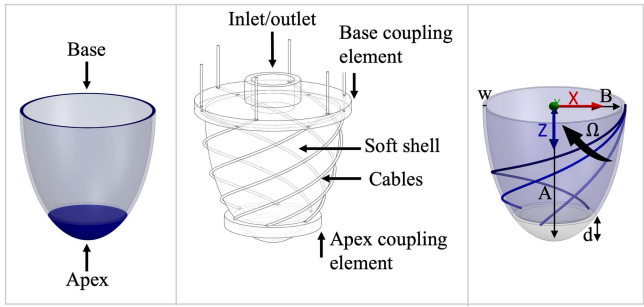

Fig. 2. (a) Soft shell design. (b) Cable-driven soft pump implementation: The soft shell, the cables, and the two rigid coupling elements at the base and at the apex. (c) Geometrical parameters: Semimajor axis A, semiminor axis B, apex height d, and shell thickness w. Three actuators with increasing Ω (equal to 2, 4, and 6).

aimed at replicating the heart function in simulators employed for medical training or used as preliminary testing platforms for cardiovascular devices [17]. However, the research on soft pumps also holds the future potential for deployment as artificial hearts, either for partial or complete organ replacement [18]. To mimic the pumping of human heart ventricles, the so far reported soft pumps exploited traditional actuation principles, such as the pressurization of foam-based actuators [19], or deformable pouches [20], [21] enclosed within bioinspired cases [22]. To enable a biomimetic motion, both sleeves supporting the cardiac functionality [23] and dynamic heart simulators [24], [25] relied on helically oriented structures and/or soft actuators. These state-of-the-art solutions, however, embedded the actuators into a soft, fluid-hosting chamber, leading to limited performances within the physiological range of blood pressures [25], [26].

Here, we present a novel architecture for a heart ventricle simulator where helical actuators are connected to the fluid-containing chamber only at their extremities. The body of the actuators is not bonded to the outer surface of the chamber, thus allowing the chamber to attain larger contractions. In particular, a dramatic reduction in the internal volume of the chamber occurs when it undergoes torsional buckling triggered by the helical actuators. We prove that the introduction of structural buckling is beneficial in terms of pumping capabilities.

Our work sets the ground for the exploitation of mechanical instabilities as innovative working strategies for a new generation of soft pumps that will find application in several fields, such as medical rehabilitation [27], [28] and artificial organs [29].

II. Materials and Methods

A. Actuation Concept

In this work, a soft pump based on a novel actuation principle is described. The main concept is about the possibility to take advantage of torsional buckling to improve ejection performance. The main body of the soft pump is a thin semiellipsoidal elastomeric shell that can undergo mechanical instabilities if subject to torsional stresses, leading to inward deformation. More specifically, if a torsion is applied (e.g., by cables or fluidic actuators), helicoidal inward folds are generated and as a result, the internal volume dramatically decreases [see Fig. 1].

Preliminary considerations were made to exclude a more obvious loading condition (such as a longitudinal load) may be more effective than a torsional load, with the aid of computational simulations. The semiellipsoidal shell was subjected to a load, either a simple rotation (for producing torsion), or an axial displacement (for producing longitudinal loading). The simulations were performed at equal strain energy $E = 1$ J and the deformed configurations were compared in terms of volumetric reduction. The results showed the key role of torsion in the formation of folds that remarkably contribute to the variation of the inner volume of the shell. This preliminary result paved the way for further investigation of the torsional loading.

B. Design and Fabrication

The semiellipsoidal shell has semimajor axis $A = 60$ mm, semiminor axis $B = 30$ mm, and thickness $w = 1.5$ mm. At a distance of 50 mm from the base plane, the shell is filled with material, constituting the shell apex [see Fig. 2(a)]. The shell was fabricated by casting silicone in a 3-D-printed mold (Figs. S1 and S2, Supplementary). The soft silicone Ecoflex 00-30 - EF30 (Smooth-On Inc.), and the medium soft silicone Smooth-Sil 950 - SS950 (Smooth-On Inc.) were employed in the fabrication of two shell prototypes with different stiffness.

Although the principle can be implemented with any linear actuator that can generate a helical contraction, in this work, cables pulled by an external actuation system have been preferred for simplicity and effectiveness in demonstrating the concept. Thus, the soft shell is surrounded by a variable number of cables, helically disposed. These cables are attached to the soft shell solely at the base and at the apex through two 3-D-printed rigid parts. They were designed to link the cables to the shell and to set their angles and positions at the base and at the apex, through small directional holes created in the two parts [see Fig. 2(b)]. This design choice leaves the central portion of the shell free to deform, with the generation of unconstrained folds.

C. Geometrical Model

A geometrical model was developed to estimate the displacement of the shell apex relative to the base, upon actuation [see Fig. 2(b)]. The friction between the cables and the rigid part at the base is neglected in our model. As a simplifying

hypothesis, the geometrical disposition of the cables around the soft shell is considered helical throughout the cables pulling, with no variation in the pitch angle of the helix. Additionally, the interaction between the cables and the external surface of the deforming soft shell is neglected.

In the current implementation, cable pulling decreases the portion of the cables comprised between the base and the apex coupling elements, replicating the effect of contracting actuators. In this model, we consider that the extremity of each actuator is fixed at the base, while the other is attached to the rigid structure at the apex.

The outer surface of the shell is described by the Cartesian parametric equations of a semiellipsoid

$$\begin{cases} x = (B+w)\cos\psi\cos\alpha \\ y = (B+w)\cos\psi\sin\alpha \\ z = (A+w)\sin\psi \end{cases} \tag{1}$$

where w is the thickness of the shell, A and B are the semimajor and the semiminor axes, respectively, $\psi \in [0, \pi/2]$ and $\alpha \in [-\pi, \pi]$. We describe the configuration of the actuators as elliptical helices belonging to the outer surface of the shell. By substituting $\psi = t$ and $\alpha = \Omega\, t$ in (1), the Cartesian parametric equations of a semiellipsoidal helix read

$$\begin{cases} x = (B+w)\cos t\cos\Omega\, t \\ y = (B+w)\cos t\sin\Omega\, t \\ z = (A+w)\sin t. \end{cases} \tag{2}$$

The helix parameter Ω determines n, which is the number of turns of the helix around the semielliptical surface, specifically $n = \frac{\Omega}{4}$ [see Fig. 2(c)]. By knowing the apex height d, the coordinates of one helix are described by (2), where $t \in [0, t_0]$ and $t_0 = \arcsin\left(\frac{(A+w)-d}{A+w}\right)$.

To track the position of the apex, we follow the displacement of the point of attachment between one actuator and the apex. Before contraction, the coordinates of this point are (x_0, y_0, z_0), obtained from (2) when $t = t_0$. Also, the initial length L of one actuator is computed from (2) as

$$L = \int_0^{t_0} \sqrt{((B+w)\sin t)^2 + ((A+w)^2 + (B+w)^2\Omega^2)(\cos t)^2}\; dt. \tag{3}$$

The actuator shortening can be defined as $C = (L-l)/L$ where l is the actuator length after contraction. By knowing the amount of shortening, the following nonlinear equation can be solved for t_f:

$$l = \int_0^{t_f} \sqrt{((B+w)\sin t)^2 + ((A+w)^2 + (B+w)^2\Omega^2)(\cos t)^2}\; dt \tag{4}$$

where $t \in [0, t_f]$ is used in (2) for the description of the helix when the actuator is contracted. Indeed, if the helical actuators were free to contract along their axes, their extremities at the apex would follow the same helical trajectories. Thus, the coordinates of the point of attachment between one actuator and the apex at the end of contraction may be estimated as

$$\begin{cases} x_f = R_0\cos(\Omega\, t_f) \\ y_f = R_0\sin(\Omega\, t_f) \\ z_f = (A+w)\sin t_f \end{cases} \tag{5}$$

where $R_0 = (B+w)\cos t_0$ is the radius of the rigid structure at the base.

Finally, the axial translation Δz and the rotation $\Delta\alpha$ of the apex with respect to the z-axis are simply obtained as

$$\Delta z = z_f - z_0 \tag{6}$$

$$\Delta\alpha = \Omega(t_f - t_0). \tag{7}$$

D. Finite Element Model

Buckling is the sudden deformation of a structural member that is loaded in compression. This is a typical phenomenon in thin membranes and columns, when subjected to an axial load exceeding a critical value. Buckling is characterized by a noticeable departure from the original stable equilibrium path when the applied load is incrementally increased [30]. A standard thin-walled structure under these conditions is described by a prebuckling state and a postbuckling state [31]. The critical buckling load is the load level at which the prebuckling state becomes unstable, and another equilibrium state is found (postbuckling). The prediction of the postbuckling behavior of structures can find an exact analytical solution only for specific simple geometries and boundary conditions [30]. To solve complex buckling problems, computational methods such as finite element analyses are commonly employed [32]. In the literature, a solution strategy in finite element models (FEMs) is the introduction of geometrical imperfections that perturb the geometry of the structure and select the postbuckling state that is experimentally observed [8], [16], [33].

In our study, we implemented a nonlinear static FEM in the ANSYS Workbench 2019R3 to study the postbuckling of the soft shell upon contraction of the actuators, and to evaluate the volume and shape changes in the structure. The buckling of the soft shell is studied with a preliminary simulation in the Supplementary, Fig. S3.

The initial geometry of the shell is a semiellipsoid with semimajor axis $A = 60$ mm, semiminor axis $B = 30$ mm, and thickness $w = 1.5$ mm [see Fig. 2(a)]. The silicone material of the shell was modeled using the third-order Yeoh strain energy function, whose parameters were $C_{10} = 0.35944$ MPa, $C_{20} = -0.14221$ MPa, $C_{30} = 0.261123$ MPa, and $D_1 = D_2 = D_3 = 0$ MPa^{-1}. The material parameters were experimentally determined through specific material characterization tests [34]. In particular, three standard dog-bone samples were cyclically tested with a Universal Testing Machine (INSTRON 5965, Norwood, MA, USA) under tensile deformation up to 50% strain at a velocity of 50 mm/min, over 5 cycles of loading and unloading.

As a simplifying hypothesis, the shortening of the actuators was accounted for by imposing a displacement to the external surface of the shell apex, with respect to the fixed base. In detail, the boundary conditions of axial translation and rotation were evaluated from the geometrical model presented in the previous

section, and applied to the apex. The FEM aims at describing the contracted soft shell by considering the configuration of the apex when the contraction of the actuators is completed, and the trajectory followed by the apex in experiments was neglected.

A parametric study was carried out to predict the shell deformation, when Ω was varied between 1 and 5, while the actuators were contracted by 20, 30, 40, 50, and 60% (corresponding to the parameter $C = 0.2$, 0.3, 0.4, 0.5, and 0.6, respectively). From the results of the simulations, the number of folds formed in the soft shell was visually evaluated, while its volumetric reduction was computed by exporting the geometry into SolidWorks (Dassault Systámes, SE).

A detailed study of the postbuckling behavior of the soft shell was carried out in ANSYS 2019R3, selecting the cases $\Omega = 4$ and $C = 0.4$. Three subsequent finite element analyses were performed.

1) Analysis A1: First static structural in which a small prestress is applied to the shell, using the following boundary conditions:
   a) fixed ring surface at the base of the shell;
   b) blocked axial translation of the apex along the longitudinal axis (Z);
   c) 1° rotation of the shell apex around the longitudinal axis (Z).
2) Analysis A2: Linear buckling performed to compute the buckling mode-shapes of the prestressed shell. We verified that the eigenvalues are closely spaced, as it is typical of imperfection sensitive structures.
3) Analysis A3: Second static structural performed on the shell seeded with the geometrical imperfections. One mode, or a combination of modes, were introduced as small geometrical imperfections in the semiellipsoidal shell, to guide the formation of the folds. Those imperfections were scaled by a factor Ψ, whose value was varied between 1 and 0.025 to assess the sensitivity of the result to the amplitude of the introduced geometric perturbation. The following boundary conditions are given by the geometrical model and they are relative to the configuration $\Omega = 4$ and $C = 0.4$:
   a) fixed ring surface at the base of the shell;
   b) $\Delta z = 19.8$ mm, apex translation along the longitudinal axis ($-Z$);
   c) $\Delta\alpha = 99.8°$, apex rotation around the longitudinal axis (Z).

The self-contact on the internal surface of the shell and on the external surface of the shell was modeled. Numerical damping was introduced via the parameter energy dissipation ratio (EDR). As a general rule, to achieve good accuracy, it is desirable to set the EDR to the lowest possible value that still allows the convergence of the simulation. We used a constant damping, that was activated on not convergence only. Also, the damping parameter was adjusted during the solution, according to the level of difficulty in convergence, making use of the restart option. From the final result, the number of folds in the deformed shell shape was evaluated and compared to experiments.

To decrease the computational cost of the postbuckling analysis in the parametric study, a simplified approach was used. In the analysis A1, boundary condition number 3 was modified to apply a 23.5° rotation to the apex of the shell. This strategy allowed us to skip A2 and obtain the desired deformed shape of the shell in the structural analysis A3, with a minimal damping. In A3, a scaling factor $\Psi = 1$ was employed and the maximum directional deformation of the soft-shell was evaluated. The normal Lagrange algorithm was used for the self-contacting surfaces to get a maximum penetration that was close to zero. The load path was chosen to minimize the number of simulation steps. When two or three simulation steps were used, the EDR was set to 0.0001, while in the cases of one single simulation step, the EDR was 0.001. We verified that the results are independent from the load path imposed in A3. Three different combinations of apex rotation and translation were explored, always reaching one target final configuration (99.8° of apex rotation and 19.8 mm of apex translation). These loads were applied either in one single step, two steps, or four steps. The default nonlinear mechanical mesh was employed (default element size equal to 5.413 mm). A mesh refinement was performed to confirm the results and a body sizing with mesh seed 3 mm was applied. Also, a smaller scaling factor ($\Psi = 0.1$) was used to introduce a smaller radial perturbation that was evaluated with respect to the thickness of the shell.

Finally, the developed FEM was employed to evaluate the efficiency (as the ratio between the input mechanical work and the output hydraulic work) and to compare the case of a longitudinal ($\Omega = 0$) and a helical actuation ($\Omega = 4$) at equal actuator contraction ($C = 0.4$). The calculation details are reported the Supplementary.

E. Experimental Validation

To validate the geometrical model, the predictions of the translation and rotation of the shell apex, for different values of the shortening of the actuators, were compared with experimental results in the case of $\Omega = 4$. To this aim, a custom-made setup was built, as depicted in Fig. 3(a) and (b). The soft shell was surrounded by inextensible cables, that were pulled by a Universal Testing Machine (INSTRON 5965, Norwood, MA, USA), simulating the actuators shortening C. To investigate the model sensitivity to the stiffness, two materials (EF30 and SS950) were employed for the fabrication of two different shells by casting. Three prototypes per material were tested over three trials for each value of the parameter C. The shell prototype was glued (Sil-Poxy, Smooth-On Inc.) at the base and at the apex to two 3D-printed rigid parts (VisiJet M3 Crystal MJP, 3D Systems Inc., Figs. S4 and S5, Supplementary). Both the rigid parts present holes to fix the orientation of six nylon cables that were passed through and held with a knot at the apex. On the other side, each cable was fixed to a plexiglass disk, whose vertical translation was controlled by the crosshead of the Universal Testing Machine. The rigid part at the base of the soft shell was fixed with screws to a Plexiglass frame, rigidly connected to the base of the Universal Testing Machine. Thus, the length of the cables between the base and the apex of the shell, corresponding to different values of shortening of the actuators, was set by moving upward the machine crosshead.

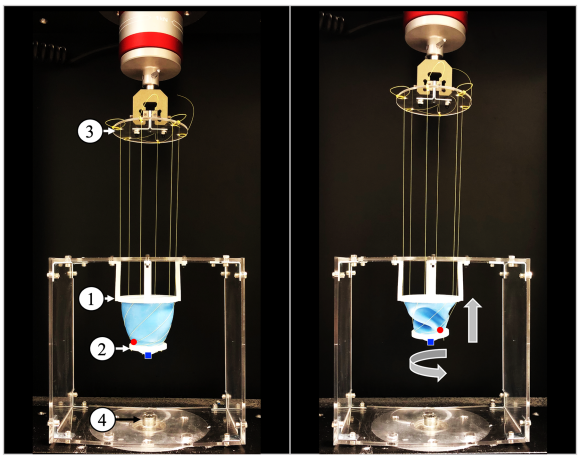

Fig. 3. Experimental setup for the validation of the geometrical model. (a) Rest position. (b) Contracted position after pulling the cables. The red and the blue markers are position sensors, 1) rigid part at the base of the soft shell, 2) rigid part at the apex of the soft shell, 3) Plexiglass disk, 4) connection between the Plexiglass frame and the base of the Universal Testing Machine.

The displacement of one cable at the apex was tracked by using a position sensor (Aurora Micro 6DOF Sensor Tool, 0.8×0.9 mm, NDI Aurora and Measurements) [see Fig. 3(a) and (b), red circle marker] and a reference position sensor under the apex (Aurora 6DOF Reference, 25 mm Disc Standard, NDI Aurora and Measurements) [see Fig. 3(a) and (b), blue square marker]. The volumetric reduction of three prototypes per material was evaluated, at different shortening values of the actuators. The volumetric reduction was evaluated through the ejection fraction, defined as $EF = (1 - \frac{V_c}{V_u})100$, where V_u and V_c are the inner volumes of the undeformed and the contracted shells, respectively. The inner volume was experimentally evaluated by filling the shell with water and measuring the amount with a syringe.

The FEM was validated by evaluating both the volumetric reduction and the contracted shape, in terms of number of folds. A custom-made setup was built to replicate the FEM boundary conditions [Fig. 4(a)]. The apex of the shell was glued (Sil-Poxy, Smooth-On Inc.) to a 3-D-printed knob (VisiJet M3 Crystal MJP, 3D Systems Inc.) that remains free to rotate around the vertical axis, while its base was glued (Sil-Poxy, Smooth-On Inc.) to a Plexiglass sled that is free to axially translate. The contracted configuration was obtained by rotating the knob and translating the sled, according to the boundary conditions imposed in the model [see Fig. 4(b)]. For each configuration, the number of inner folds was evaluated by visual inspection, while the EF was measured as previously described. Three SS950 prototypes fabricated by casting were tested over three trials for each of the nine configurations of interest, that were selected as validation cases.

F. Artificial Ventricle Simulator

A cable-driven soft pump was built to investigate its application as an artificial heart ventricle simulator. The aim of this

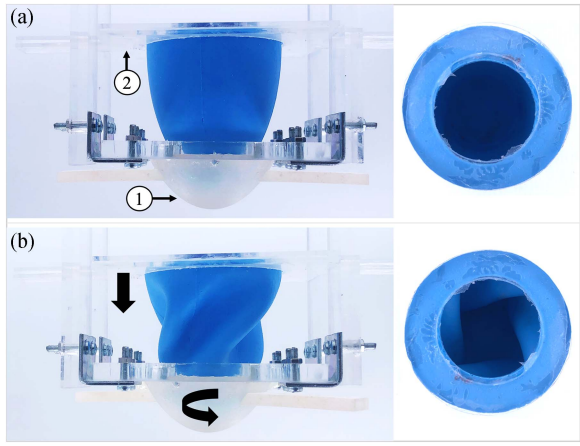

Fig. 4. Experimental setup for the FEM validation. (a) Undeformed configuration, front (left), and top view (right). (b) Contracted configuration, front (left), and top view (right). 1) 3D-printed knob at the apex, 2) Plexiglass sled at the base.

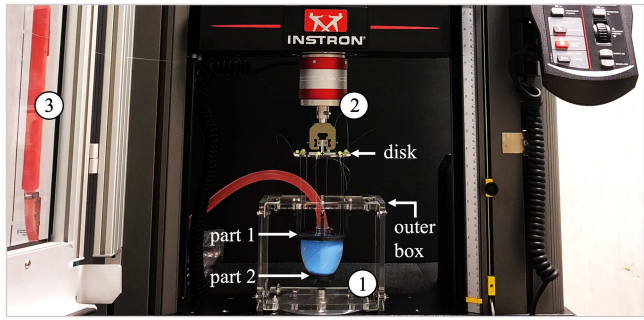

Fig. 5. Artificial ventricle simulator. 1) Artificial ventricle with the cable-driven system in the rest state. Parts 1 and 2 are rigid coupling elements between the soft shell and the cables, at the base and at the apex, respectively. 2) 1000 N load cell and gripper fixed to the Plexiglass disk to pull the cables. 3) Water column connected to the base of the artificial ventricle through a silicone tube.

case study is to verify whether the pump is able to reproduce a physiological performance when subject to physiological values of afterload pressure. The setup shown in Fig. 5 was employed to actuate the soft shell by pulling the Plexiglass disk holding the cables at a fixed speed. Concurrently, the pulling force was recorded from the Universal Testing Machine (INSTRON 5965, Norwood, MA, USA). Cables were arranged around the shell as helices with $\Omega = 4$ and the imposed displacement of the Plexiglass disk corresponded to 40% of the cable length ($C = 0.4$). The dimensions $A = 60$ mm and $B = 30$ mm of the soft shell were specifically chosen to accommodate a water volume of 108.6 ml, which falls within the normal range of the end-diastolic left ventricular volume in humans [25], [35]. Physiological afterload pressures were simulated with a water column, whose height was adjusted to apply 30, 60, and 90 mmHg at the ventricle base level [21], [29]. The minimum and maximum afterload pressures were selected with reference to average physiological values. In particular, 30 and 90 mmHg are comparable to the maximum pulmonary aortic pressure for the right ventricle, and the mean aortic pressure for the left ventricle, respectively [29].

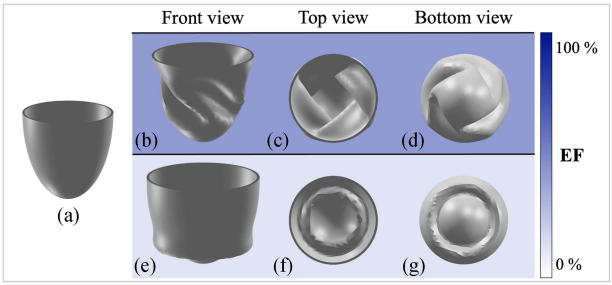

Fig. 6. (a) Undeformed shell; contracted shell in the case of helical actuation (b)–(d) and longitudinal actuation (e)–(g). A color bar gives an indication on the percentage of volumetric reduction of the contracted shell with respect to the undeformed shell.

To assess the performance of the soft pump, both static and dynamic tests were carried out. In the static tests, the stroke volume (i.e., the volume of the ejected liquid - SV) was evaluated at varying afterload pressure by measuring the rise of the water level in the column and repeating the test three times, for each afterload pressure (30, 60, and 90 mmHg). Dynamic tests were also conducted by pulling and releasing the cables in 2 s at 3000 mm/min (30 bpm), over ten cycles. The water level displacement was assessed from a video analysis (Tracker Video Analysis, Physlet.org), to record the dynamic SV at varying afterload pressure. Additional details on the setup and the experimental protocol are given in the Supplementary.

In addition, from the experimental data acquired during the dynamic testing of the pumped volume of fluid against afterload pressure, and of measured force versus displacement of the cables, the efficiency of the cable-driven soft pump was computed at varying afterload pressure. In details, the efficiency is $e = \frac{H}{M}$, where H is the output hydraulic work and M is the input mechanical work. The hydraulic work is $H = P_a\ SV$, where P_a is the applied afterload pressure and SV is the average maximum stroke volume, over nine cycles. The mechanical work M is the integral of the mean curve over nine cycles of the measured force with respect to the displacement of the cross head, calculated during the pulling phase of the cables.

III. Result and Discussion

A. Actuation Concept

Preliminary finite element simulations were made to highlight the critical role of torsional buckling of the chamber induced by helical actuators in maximizing its volumetric reduction. Indeed, helical actuators allow for a volumetric reduction of 42% [see Fig. 6(b)–(d)] as compared to 12% obtained using longitudinal actuators [see Fig. 6(e)–(g)], while maintaining the same strain energy. These preliminary results directed the following studies for the optimization of the pumping performances of our soft device. In particular, the helicoidal disposition of the cables was preferred to impose a torsional loading to the soft shell.

B. Geometrical Model and Experimental Validation

The prediction of the translation and rotation of the apex according to the geometrical model for different values of the shortening and the parameter Ω are plotted in Fig. 7. The results are relative to a semiellipsoidal shell having $A = 60$ mm, $B = 30$ mm, $w = 1.5$ mm, and $d = 10$ mm. The modeled rotation and axial translation of the apex are plotted for different values of Ω and shortening C. As expected, both quantities increase with the increasing shortening of the actuators. In addition, the geometrical arrangement of the actuators determined by the parameter Ω has a stronger effect on the apex rotation than on the axial translation. The apex rotation is linearly related to Ω.

The graphical comparison between the trajectory of one cable at the apex evaluated by the geometrical model and experimentally shows good agreement [see Fig. 7(b)]. For the soft shell [see Fig. 7(b), upper row], both the axial translation and rotation are well captured by the geometrical model, and the mean error is 1.2 mm and $-7°$ only, respectively. When the shell is made of the medium soft silicone [see Fig. 7(b), bottom row], the axial translation is still well estimated by the geometrical model (mean error 0.8 mm), while the error on the rotation increases (mean error $-23.0°$). With the increasing stiffness of the shell, the trajectory of the cables at the apex measured experimentally deviates from that computed using the geometrical model.

The presented experimental results show the limitations of the geometrical model in predicting the displacement of the shell apex relatively to the base when varying the constitutive material of the soft shell. The model has very good agreement with the experiments for shells made of soft materials, since the disposition of the cables around the shell remains helical during cables pulling, and the points of interaction between the cables and the external surface of the soft shell are limited [see Fig. S6(a) and (c), Supplementary]. When the soft shell is made of a stiffer material, the increased tension in the cables to deform the soft shell makes the cables assume a configuration that deviates from the helical one, also with an increased interaction with the deformed soft shell [see Fig. S6(b) and (d), Supplementary].

C. Finite Element Model and Experimental Validation

The postbuckling behavior of the soft shell prototype under torsional instability is determined by the imperfections introduced during the fabrication process. With the simple fabrication using casting in 3-D-printed molds, we have no precise control over the defects, but we suggest that the four parts that constitute the mold might play a role in determining the buckled shape. Indeed, during experiments, we identified the fourfold shape as the preferred deformation of the soft shell, when subjected to torsion. As anticipated, in the simulations, we tried different buckling modes or combinations of them, until we found the perturbation that produced the configuration matching the observed one.

In our study, buckling mode 7 was selected. In Fig. 8(a), the radial displacement of the shell relative to mode 7 is shown. Qualitatively, this pattern is recognizable as an incipit for the formation of four folds. Indeed, when the buckling mode 7 was used with a scaling factor $\Psi = 0.025$, the result of A3 is a deformed shell with four folds [see Fig. 8(b)]. We verified that the geometrical imperfection introduced are small, since they only represent 1.7% of the soft-shell thickness. In this specific

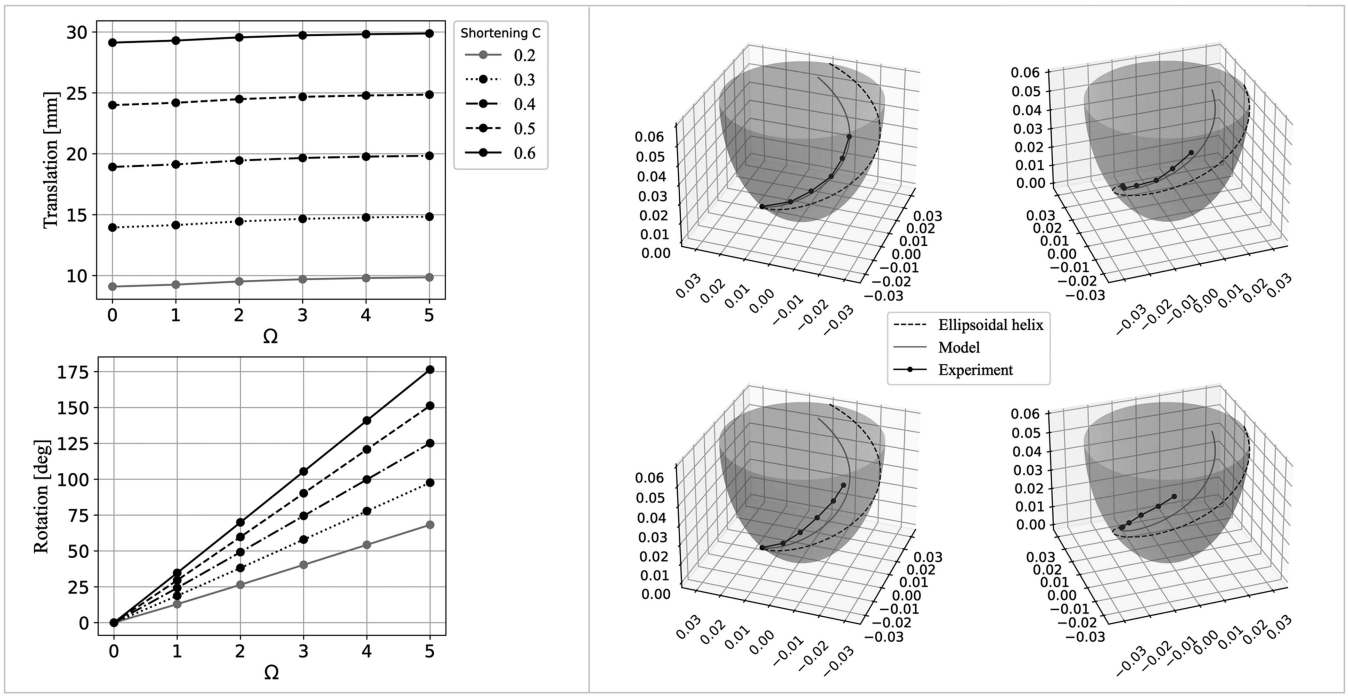

Fig. 7. (a) Geometrical model results, at variable Ω and shortening C: Axial translation [mm] (top) and axial rotation [deg] (bottom). (b) Comparison between the trajectory of the pulled cables predicted by the geometrical model (gray line) and experimental tests (black line) with the soft shell (EF30) prototype (upper row) and the medium soft (SS950) prototype (bottom row) in two different views. The black dashed line describes the helical disposition of the cable around the shell at rest.

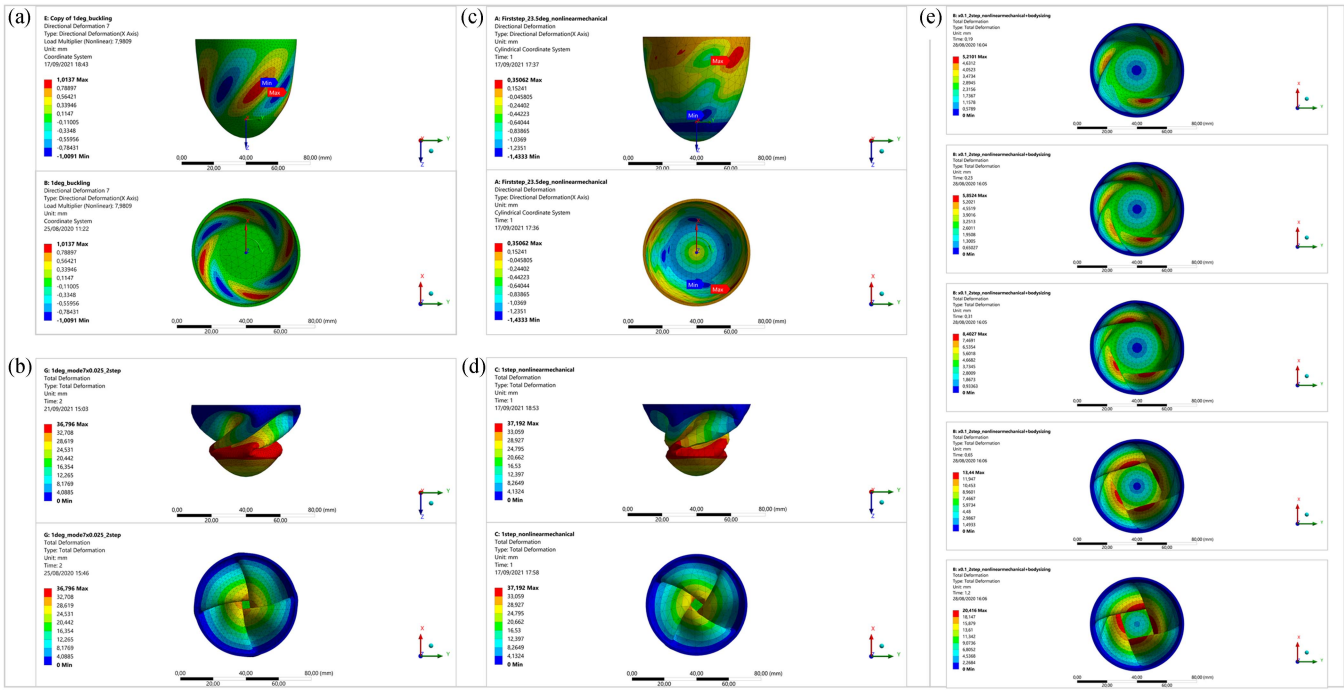

Fig. 8. FEM results. (a) Linear buckling analysis A2, mode 7, directional deformation (X), front view and top view. (b) Static structural analysis A3, total deformation, front view, and top view. (c) First static structural analysis A1, directional deformation (X), front view, and top view. (d) Second static structural analysis A3, total deformation, front view, and top view. (e) FEM results at different time points (total solution time 2 s): $t = 0.19$ s, three folds; $t = 0.23$ s, six folds; $t = 0.31$ s, four folds and two smaller ones; $t = 0.65$ s, four folds and two smaller ones; $t = 1.2$ s, four folds.

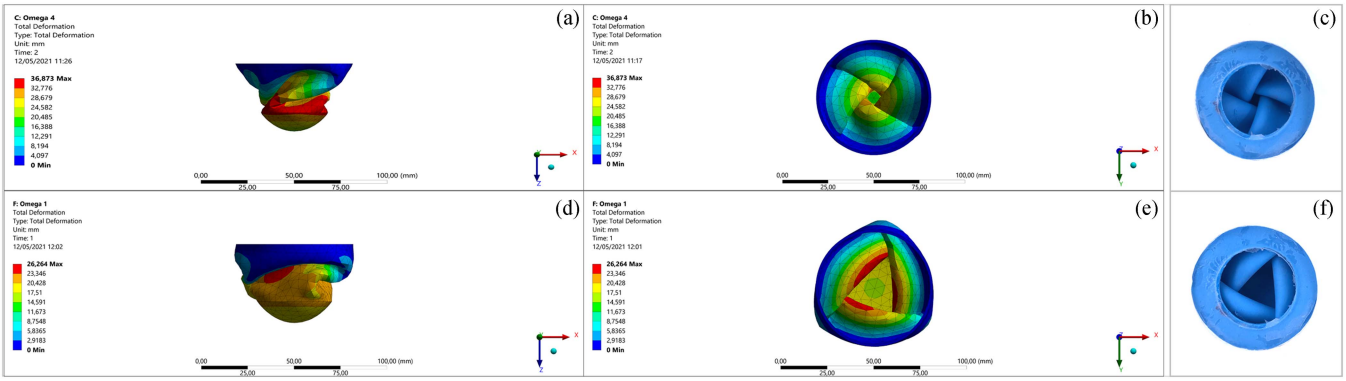

Fig. 9. FEM results of the deformation of the shell in the case where four folds form ($\Omega = 4$ and $C = 0.4$), (a) front and (b) top view, and in the case of three folds formation ($\Omega = 1$ and $C = 0.4$), (d) front and (e) top view. Experimental results in the case of (c) four folds and (f) three folds, top views.

TABLE I
FEM PARAMETRIC STUDY

EF (folds)	$\Omega = 1$	$\Omega = 2$	$\Omega = 3$	$\Omega = 4$	$\Omega = 5$
$C = 0.2$	32.8 (4)	36.4 (4)	51.4 (4)	55.7 (4)	59.5 (4)
$C = 0.3$	41.7 (4)	55.5 (4)	63.7 (4)	67.8 (4)	70.1 (4)
$C = 0.4$	59.9 (3)	66.0 (4)	72.5 (4)	75.2 (4)	77.2 (4)
$C = 0.5$	62.2 (3)	74.4 (4)	80.6 (4)	81.8 (4)	87.5 (4)
$C = 0.6$	68.3 (3)	82.1 (4)	85.7 (4)	87.5 (4)	89.2 (4)

TABLE II
EXPERIMENTAL VALIDATION

EF (folds), error [ml]	$\Omega = 1$	$\Omega = 2$	$\Omega = 3$	$\Omega = 4$	$\Omega = 5$
$C = 0.2$					60.5 (4) 1.9
$C = 0.3$				68.8 (4) 1.3	
$C = 0.4$	58.3 (3) 3.7	67.0 (4) 1.9	73.8 (4) 1.6	77.2 (4) 2.3	79.0 (4) 2.0
$C = 0.5$		74.0 (4) 0.4			
$C = 0.6$	71.6 (3) 3.0				

simulation, the maximum EDR was 0.01, the default nonlinear mechanical mesh was employed and a refinement of the external surface of the shell was set. In total, the model had 22 112 nodes and 10 934 elements.

To decrease the computational cost of the postbuckling analysis in the parametric study, a simplified approach was used. In analysis A1, a rotation of 23.5° was applied to the apex of the soft-shell. The corresponding radial displacement is shown in Fig. 8(c), and a deformation pattern resembling four folds was found. With a scaling factor $\Psi = 1$, the maximum directional deformation was 1.43 mm, a value comparable to the thickness of the shell. The model had 6179 nodes and 3098 elements. In A3, the target configuration was reached with a maximum number of steps equal to three. The result of one case of study ($\Omega = 4$, $C = 0.4$, and one single simulation step) is shown in Fig. 8(d).

A mesh refinement was also performed to confirm the results, obtaining a model with 17 106 nodes and 8874 elements. Also, when the scaling factor was reduced ($\Psi = 0.1$), the introduced radial perturbation represented 9.5% of the thickness of the soft-shell. It was interesting to observe that the introduced geometric imperfection is small enough to let the model explore various configurations with three and six folds, before finding the equilibrium on a configuration with four folds. A sequence of snapshots corresponding to increasing values of the load parameter is shown in Fig. 8(e).

The results of the FEM parametric study are presented in Table I, reporting the ejection fraction and the number of folds formed for each combination of Ω and C, which set the geometry and the shortening of the actuators, respectively. We obtained very good results of shell volumetric reduction, reaching a $EF > 50\%$ in most of the cases of study. We noticed that the volumetric reduction increases both with the number of turns that the actuators make around the shell and their shortening. The number of folds in the deformed configuration of the shell is generally four, but the combinations $\Omega = 1, C = 0.4$ and $\Omega = 1$, $C = 0.6$ show an interesting transition toward three folds. Fig. 9 shows the deformed configurations of the shell at the end of contraction, for two typical cases where three and four folds appear. It is worth to underline that these results highlight the quality of our FEM. Indeed, even thought geometrical imperfections were introduced to guide the deformation toward four folds in the contracted shape, those imperfections are small enough, and the model is also able to capture final shapes that show a different number of folds.

The comparison of the FEM results with experiments allowed us to validate our model and show its good accuracy. In Table II, the experimental volumetric reduction EF and the experimental number of folds are reported, for direct comparison with Table I. Also, Table II shows the absolute error in ml between the experimental and the FEM inner volumes of the soft-shell. Both the ejection fraction and the number of folds are very well captured by the model, as also shown in Fig. 9(c) and (f). The mean error in the inner volume prediction at the end of contraction is 2 ml only (1.9% of the initial volume). The highest errors are 3.7 and 3 ml, registered in the edge cases $C = 0.4$ and $C = 0.6$ for $\Omega = 1$, respectively.

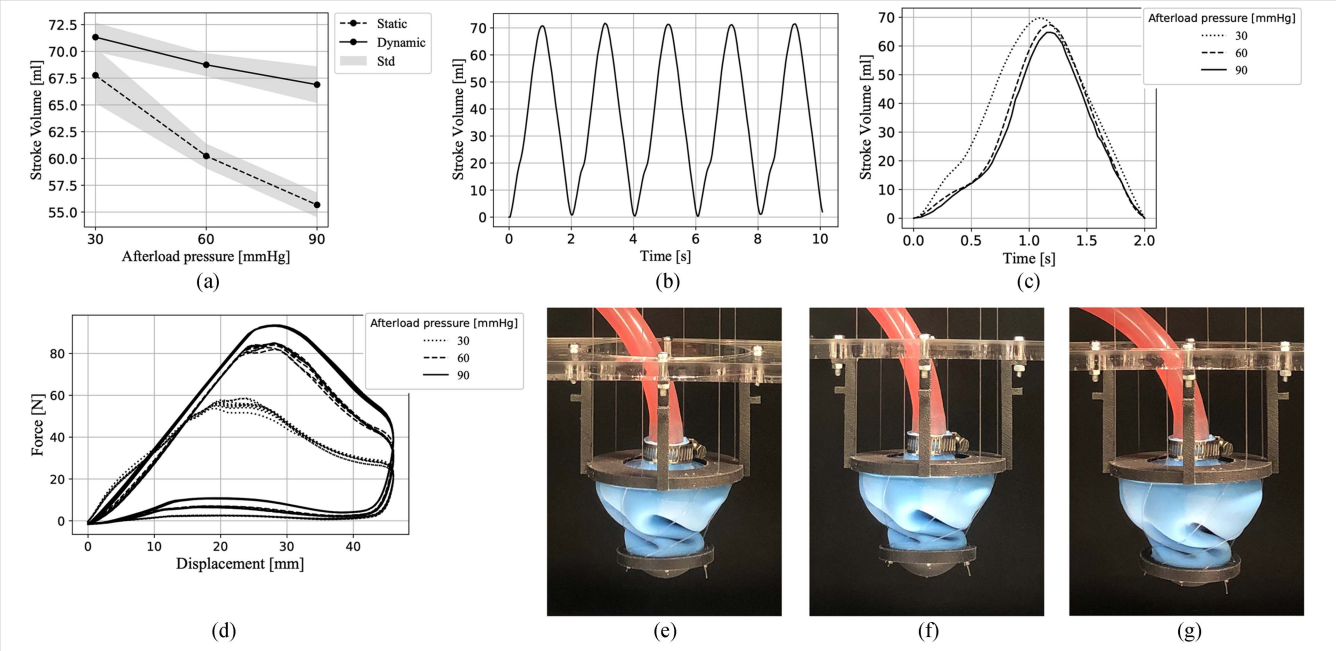

Fig. 10. Artificial ventricle simulator performance. (a) Static and dynamic peak stroke volume at varying afterload pressure. (b) Dynamic stroke volume versus time when the afterload pressure is 30 mmHg. (c) Average dynamic stroke volume versus time at varying afterload pressure. (d) Force-displacement plot, nine cycles of contraction, and relaxation at variable afterload pressure. Contracted shape of the artificial ventricle simulator at different afterload pressures: (e) 30 mmHg, (f) 60 mmHg, and (g) 90 mmHg.

As discussed in the geometrical model validation, the contraction path of the SS950 shell slightly deviates from the geometrical model prediction. However, we verified that the two main aspects of interest, that are the number of folds and the ejection fraction, are not significantly affected by the error on the predicted apex rotation $\Delta\alpha$. As reported in Table S1 (Supplementary), the average error on the predicted volume is 1.9 ml only, and the shell shape is always captured.

The system efficiency e computed using the FEM model highlighted that the helical actuation is also advantageous from an energetic point of view ($e = 0.442$) with respect to the longitudinal actuation ($e = 0.331$). Indeed, while the mechanical work required to deform the soft shell with helical actuators is 2.8 times higher than the one needed with longitudinal actuators, the output hydraulic work becomes 3.7 times, thanks to the peculiar deformation mode driven by torsional instabilities.

D. Artificial Ventricle Simulator

In Fig. 10(a), the maximum static and dynamic SVs are plotted against the applied afterload pressure and are both within the physiological range (widest range 50 ml – 100 ml, the typical value is 70 ml for a healthy heart at rest) [35], [36]. In particular, the static SV is 67.8 ± 2.6 ml, 60.2 ± 1.2 ml, and 55.7 ± 1.2 ml while the dynamic SV is 71.3 ± 1.4 ml, 68.7 ± 1.1 ml, and 66.9 ± 1.7 ml, for afterload pressures of 30, 60, and 90 mmHg, respectively. As expected, the dynamic and the static SV decrease with increasing afterload pressure. Indeed, as observed both experimentally and in simulation, the volume contained in the ventricle simulator at the end of contraction (end-systolic volume, ESV) increases with the applied afterload, especially in correspondence with the base of the shell [see Fig. 10(e)–(g)]. In addition, the dynamic stroke is always greater than the static one, suggesting that the dynamic effects arising during the contraction of the soft shell promote volume reduction through the formation of inner folds. In this regard, we expect that actuating the ventricle simulator at 60 bpm (physiological standard heart rate) the amount of pumped volume of water per beat would even increase. This implies that in dynamic conditions physiological strokes could be achieved with an even reduced actuator contraction. Fig. 10(b) reports the dynamic SV as a function of time, when the afterload pressure is set to 30 mmHg, and it shows good repeatability of the pattern over five cycles of contraction and relaxation. The mean dynamic SV with respect to time over nine cycles at different afterload pressures is shown in Fig. 10(c). In this plot, shortly after the beginning of the contraction, we observe changes in the slopes of the curves that are most likely related to the onset of the torsional instability.

During the contraction of the artificial ventricle simulator, the force profile was also recorded [see Fig. 10(d)]. The force increases almost linearly with the applied displacement, until reaching its peak, and then decreases as the inner folds appear. This behavior is typical of the torsional instability, as also confirmed numerically. The peak force was calculated as the maximum of the average curve over nine cycles and resulted to be 54.4 ± 1.6 N, 84.2 ± 1.1 N, and 93.3 ± 0.2 N at 30, 60, and 90 mmHg of applied afterload pressure, respectively.

The efficiency of the artificial ventricle simulator was calculated from the experimental data, and it is 0.168, 0.246, and 0.301 at 30, 60, and 90 mmHg, respectively. Since the system efficiency increases with the afterload pressure, the optimal working point of the soft pump could be even at higher afterload pressures.

IV. Conclusion

We had presented a soft pump based on a novel compliant mechanism, i.e., triggering a torsional instability of the pumping chamber through the action of helical actuators. We had shown that such an actuation mechanism was energetically advantageous, and it strongly increased the ejected volume with respect to others that did not involve instabilities because it led to the formation of folds in the chamber that allowed for a lever effect leading to a more significant volumetric reduction. The mechanical interaction between the actuators and the chamber was a key design aspect for the effectiveness of the proposed actuation mechanism. Indeed, in contrast with previous reports where the actuators were embedded in the artificial ventricle, here, the actuators were connected to the chamber only at the base and at the apex, thus leaving the shell free to undergo large deformations [37], [25], [26].

To gather insights on the effect of the geometry and the shortening of the actuators on the deformation and the performance of the soft pump, we had introduced geometrical and FEM models, which were successfully validated against experiments using cable-driven actuation. While the geometrical model predicted the displacement of the shell apex relative to the base during actuation, the FEM model accurately described both the contracted shape and the volumetric reduction of the soft shell. The parametric analysis clearly demonstrated the high potentialities of the presented compliant mechanism in pumping.

We described a simplified FEM pipeline with general applicability that was useful to address the complex problem of finite element simulations when mechanical instabilities were involved. It is worth to underline that our models had a broad range of applicability and practical relevance. Indeed, the proposed model could be translated to the study of systems in which the soft shell had a different shape than the semiellipsoid, i.e., a cylinder or a cone. Moreover, the principles still hold if cables are replaced by other kinds of actuators that can linearly contract and act helicoidally. In our FEM, however, the mechanical interactions between the shell and the actuators were not represented. This aspect became particularly important if soft actuators were introduced, since the contractile capabilities of the actuators were strongly dependent on the interaction forces with the soft shell at the contact points. While performing the simulation using forces instead of displacements as boundary conditions was representative only of the loading condition at the beginning of the contraction of the actuators, the modeling of the complete system with cables was superfluous since we showed that the FEM model had very good agreement with experiments. A simulation of the complete system was suggested if soft actuators were used as actuating elements. However, the increased complexity of the CAD and computational cost could hinder parametric studies.

In our study, the results of a parametric study on geometry and contractile capabilities of the actuators were used to select a combination of design parameters for the development of a soft robotic ventricle simulator capable of reaching physiological values of ejection fraction. We had demonstrated experimentally that our simulator replicated the stroke volume of a human ventricle, also at physiologically relevant afterload pressures. Our experiments showed that the force needed to actuate the soft chamber in the ventricle simulator scenario was compatible with those available in the current state-of-the-art of soft actuators [38], [39], [40], [41]. Moreover, our ventricle simulator demonstrated a great advantage in terms of efficiency with respect to previously described soft pumps that were tested in physiological conditions of afterload pressure [21].

Based on the experimental evidence of the performance of our soft pump, we strongly believed that the novel actuation mechanism proposed in this article opened new avenues for the development of soft systems with improved capabilities. Indeed, the introduction of mechanical instabilities as amplifying mechanisms, not only widened the deformations optimizing the system performances, but also improved its dynamics.

From one side, this work was intended to set the ground for further investigation of possible applications, but we expected the major impact on the field of medical simulators and artificial organs. Although far from being directly used for an implantable device, achieving efficient and physiological pumping performances represented the most important milestone for the development of a soft robotic heart ventricle that met medical applicability.

References

[1] H. Abidi et al., "Highly dexterous 2-module soft robot for intra-organ navigation in minimally invasive surgery," *Int. J. Med. Robot. Comput. Assist. Surg.*, vol. 14, no. 1, 2018, Art. no. e1875.

[2] R. Deimel and O. Brock, "A novel type of compliant and underactuated robotic hand for dexterous grasping," *Int. J. Robot. Res.*, vol. 35, no. 1–3, pp. 161–185, 2016.

[3] M. Manti, A. Pratesi, E. Falotico, M. Cianchetti, and C. Laschi, "Soft assistive robot for personal care of elderly people," in *Proc. IEEE 6th Int. Conf. Biomed. Robot. Biomechatronics*, 2016, pp. 833–838.

[4] L. N. Awad et al., "A soft robotic exosuit improves walking in patients after stroke," *Sci. Transl. Med.*, vol. 9, no. 400, 2017, Art. no. eaai9084.

[5] S. Coyle, C. Majidi, P. LeDuc, and K. J. Hsia, "Bio-inspired soft robotics: Material selection, actuation, and design," *Extreme Mechanics Lett.*, vol. 22, pp. 51–59, 2018.

[6] M. Pishvar and R. L. Harne, "Foundations for soft, smart matter by active mechanical metamaterials," *Adv. Sci.*, vol. 7, no. 18, 2020, Art. no. 2001384.

[7] A. Rafsanjani, K. Bertoldi, and A. R. Studart, "Programming soft robots with flexible mechanical metamaterials," *Sci. Robot.*, vol. 4, no. 29, 2019, Art. no. eaav7874.

[8] S. Janbaz, F. Bobbert, M. Mirzaali, and A. Zadpoor, "Ultra-programmable buckling-driven soft cellular mechanisms," *Mater. Horiz.*, vol. 6, no. 6, pp. 1138–1147, 2019.

[9] A. Pal, D. Goswami, and R. V. Martinez, "Elastic energy storage enables rapid and programmable actuation in soft machines," *Adv. Funct. Mater.*, vol. 30, no. 1, 2020, Art. no. 1906603.

[10] J. T. Overvelde, T. Kloek, J. J. D'haen, and K. Bertoldi, "Amplifying the response of soft actuators by harnessing snap-through instabilities," *Proc. Nat. Acad. Sci.*, vol. 112, no. 35, pp. 10863–10868, 2015.

[11] D. Yang et al., "Buckling of elastomeric beams enables actuation of soft machines," *Adv. Mater.*, vol. 27, no. 41, pp. 6323–6327, 2015.

[12] D. Yang et al., "Buckling pneumatic linear actuators inspired by muscle," *Adv. Mater. Technol.*, vol. 1, no. 3, 2016, Art. no. 1600055.

[13] D. Yang, M. S. Verma, E. Lossner, D. Stothers, and G. M. Whitesides, "Negative-pressure soft linear actuator with a mechanical advantage," *Adv. Mater. Technol.*, vol. 2, no. 1, 2017, Art. no. 1600164.

[14] M. S. Verma, A. Ainla, D. Yang, D. Harburg, and G. M. Whitesides, "A soft tube-climbing robot," *Soft Robot.*, vol. 5, no. 2, pp. 133–137, 2018.

[15] P. Rothemund et al., "A soft, bistable valve for autonomous control of soft actuators," *Sci. Robot.*, vol. 3, no. 16, 2018, Art. no. eaar7986.

[16] J. Shim, C. Perdigou, E. R. Chen, K. Bertoldi, and P. M. Reis, "Buckling-induced encapsulation of structured elastic shells under pressure," *Proc. Nat. Acad. Sci.*, vol. 109, no. 16, pp. 5978–5983, 2012.

[17] D. Zrinscak, L. Lorenzon, M. Maselli, and M. Cianchetti, "Soft robotics for physical simulators, artificial organs and implantable assistive devices," *Prog. Biomed. Eng.*, vol. 5, no. 1, 2023, Art. no. 012002.

[18] L. G. Guex et al., "Increased longevity and pumping performance of an injection molded soft total artificial heart," *Soft Robot.*, vol. 8, no. 5, pp. 588–593, 2021.

[19] B. C. Mac Murray et al., "Poroelastic foams for simple fabrication of complex soft robots," *Adv. Mater.*, vol. 27, no. 41, pp. 6334–6340, 2015.

[20] N. H. Cohrs et al., "A soft total artificial heart–first concept evaluation on a hybrid mock circulation," *Artif. Organs*, vol. 41, no. 10, pp. 948–958, 2017.

[21] C. M. Schumacher, M. Loepfe, R. Fuhrer, R. N. Grass, and W. J. Stark, "3D printed lost-wax casted soft silicone monoblocks enable heart-inspired pumping by internal combustion," *RSC Adv.*, vol. 4, no. 31, pp. 16039–16042, 2014.

[22] H. Liu, J. Yan, Y. Zhou, H. Li, and C. Li, "A novel dynamic cardiac simulator utilizing pneumatic artificial muscle," in *Proc. 35th Annu. Int. Conf. IEEE Eng. Med. Biol. Soc.*, 2013, pp. 715–718.

[23] E. T. Roche et al., "Soft robotic sleeve supports heart function," *Sci. Transl. Med.*, vol. 9, no. 373, 2017, Art. no. eaaf3925.

[24] C. Vannelli, J. Moore, J. McLeod, D. Ceh, and T. Peters, "Dynamic heart phantom with functional mitral and aortic valves," *Proc. SPIE*, vol. 9415, pp. 8–17, 2015.

[25] E. T. Roche et al., "A bioinspired soft actuated material," *Adv. Mater.*, vol. 26, no. 8, pp. 1200–1206, 2014.

[26] U. Gulbulak and A. Ertas, "Finite element driven design domain identification of a beating left ventricular simulator," Bioengineering, vol. 6, no. 3, 2019, Art. no. 83.

[27] J. Sun, D. Zhou, J. Deng, and Y. Liu, "Development of a high flow rate soft pump driven by intersected twisted artificial muscles units," *IEEE Trans. Ind. Electron.*, vol. 70, no. 7, pp. 7153–7162, Jul. 2023.

[28] V. Cacucciolo, J. Shintake, Y. Kuwajima, S. Maeda, D. Floreano, and H. Shea, "Stretchable pumps for soft machines," *Nature*, vol. 572, no. 7770, pp. 516–519, 2019.

[29] A. X. Kohll et al., "Long-term performance of a pneumatically actuated soft pump manufactured by rubber compression molding," *Soft Robot.*, vol. 6, no. 2, pp. 206–213, 2019.

[30] S. Emam and W. Lacarbonara, "A review on buckling and postbuckling of thin elastic beams," *Eur. J. Mechanics-A/Solids*, vol. 92, 2022, Art. no. 104449.

[31] M. N. Bin Kamarudin, J. S. Mohamed Ali, A. Aabid, and Y. E. Ibrahim, "Buckling analysis of a thin-walled structure using finite element method and design of experiments," *Aerospace*, vol. 9, no. 10, 2022, Art. no. 541.

[32] C. Bisagni, "Numerical analysis and experimental correlation of composite shell buckling and post-buckling," *Composites Part B, Eng.*, vol. 31, no. 8, pp. 655–667, 2000.

[33] S. Babaee, J. Shim, J. C. Weaver, E. R. Chen, N. Patel, and K. Bertoldi, "3D soft metamaterials with negative Poisson's ratio," *Adv. Mater.*, vol. 25, no. 36, pp. 5044–5049, 2013.

[34] L. Marechal, P. Balland, L. Lindenroth, F. Petrou, C. Kontovounisios, and F. Bello, "Toward a common framework and database of materials for soft robotics," *Soft Robot.*, vol. 8, no. 3, pp. 284–297, 2021.

[35] J. J. Feher, *Quantitative Human Physiology: An Introduction*. New York, NY, USA: Academic, 2017.

[36] D. Sidebotham and I. J. Le Grice, *Physiology and Pathophysiology*, Oxford, U.K.: Butterworth-Heinemann Elsevier, 2007, p. 9.

[37] C. Park, C. Ozturk, and E. T. Roche, "Computational design of a soft robotic myocardium for biomimetic motion and function," *Adv. Funct. Mater.*, vol. 32, no. 40, 2022, Art. no. 2206734.

[38] N. S. Usevitch, A. M. Okamura, and E. W. Hawkes, "Apam: Antagonistic pneumatic artificial muscle," in *Proc. IEEE Int. Conf. Robot. Autom.*, 2018, pp. 1539–1546.

[39] M. Zhu, T. N. Do, E. Hawkes, and Y. Visell, "Fluidic fabric muscle sheets for wearable and soft robotics," *Soft Robot.*, vol. 7, no. 2, pp. 179–197, 2020.

[40] E. H. Skorina et al. Onal, "Reverse pneumatic artificial muscles (RPAMS): Modeling, integration, and control," *PLoS One*, vol. 13, no. 10, 2018, Art. no. e0204637.

[41] E. W. Hawkes, D. L. Christensen, and A. M. Okamura, "Design and implementation of a 300% strain soft artificial muscle," in *Proc. IEEE Int. Conf. Robot. Autom.*, 2016, pp. 4022–4029.

Lucrezia Lorenzon (Associate Member, IEEE) received the M.Sc. degree in biomedical engineering (*cum laude*) from the Polytechnic University of Milan, Milan, Italy, in 2018, and the Ph.D. degree in biorobotics (*cum laude*) from Scuola Superiore Sant'Anna, Pisa, Italy, in 2023.

She is currently conducting research with the Soft Mechatronics for Biorobotics Lab, The Biorobotics Institute of Scuola Superiore Sant'Anna, Pontedera, Italy, focusing on the development of implantable soft robotic solutions within the biomedical field.

Alessandro Lucantonio received the M.Sc. degree in space engineering in 2013, and the Ph.D. degree in theoretical and applied mechanics from Sapienza Universitá di Roma, Rome, Italy, in 2013.

In the past years, he was an Assistant Professor with the Biorobotics Institute, Scuola Superiore Sant'Anna, Pisa, Italy. He is currently an Associate Professor with Aarhus University, Aarhus, Denmark. His research interests include the theoretical and computational modeling of multiphysics systems.

Leone Costi received the M.Sc. degree in bionics engineering jointly from University of Pisa, Pisa, Italy, and Scuola Superiore Sant'Anna, Pisa, Italy, in 2020. He is currently working toward the Ph.D. degree in engineering with the Bio-Inspired Robotics Laboratory, University of Cambridge, Cambridge, U.K.

His research interests include embodied intelligence, soft robotics, medical robotics, and artificial organs.

Debora Zrinscak received the M.Sc. degree in mechatronic engineering from the Polytechnic University of Turin, Turin, Italy, in 2018 and the Ph.D. degree in biorobotics (*cum laude*) from the Biorobotics Institute, Scuola Superiore Sant'Anna, Pisa, Italy, in 2022.

Her main research interests include soft robotic actuation solutions and bioinspired mechatronic systems.

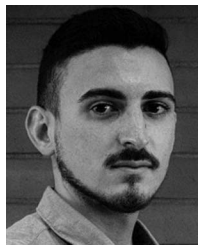

Luca Arleo received the M.Sc. degree in mechanical engineering (*cum laude*) from the Polytechnic University of Bari, Bari, Italy, in 2020. He is currently working toward the Ph.D. degree in biorobotics with the Soft Mechatronics for Biorobotics Lab, Biorobotics Institute, Scuola Superiore Sant'Anna, Pisa, Italy.

His research interests include additive manufacturing, variable stiffness, and bioinspired design.

Matteo Cianchetti (Member, IEEE) received the Ph.D. degree in biorobotics from Scuola Superiore Sant'Anna, Pisa, Italy, in 2011.

He is currently an Associate Professor with The Biorobotics Institute, Scuola Superiore Sant'Anna, Pisa, Italy, where he leads the Soft Mechatronics for Biorobotics Lab. His research interests include bioinspired robotics, soft actuators, smart compliant sensors, and flexible mechanisms.

Open Access funding provided by 'Scuola Superiore "S.Anna" di Studi Universitari e di Perfezionamento' within the CRUI CARE Agreement